Effect of slip on the contact-line instability of a thin liquid film flowing down a cylinder

Chicheng Ma,[1,2] Jianlin Liu,[1,*] Mingyu Shao,[2] Bo Li,[2] Lei Li,[2] and Zhangna Xue[1]

[1]*College of Pipeline and Civil Engineering, China University of Petroleum (East China), Qingdao 266580, China*

[2]*Department of Mechanics, School of Transportation and Vehicle Engineering, Shandong University of Technology, Zibo 255000, China*

(Received 14 June 2019; revised manuscript received 22 February 2020; accepted 17 April 2020; published 22 May 2020)

Liquid coating films on solid surfaces exist widely in a plethora of industrial processes. In this study, we focus on the falling of a liquid film on the side surface of a vertical cylinder, where the surface is viewed as slippery, such as a liquid-infused surface. The evolution profiles and flow instability of the advancing contact line are comprehensively analyzed. The governing equation of the thin film flow is derived according to the lubrication model, and the traveling-wave solutions are numerically obtained. The results show that the wave speed increases with the increase of a larger slippery length. A linear stability analysis (LSA) is carried out to verify the traveling solutions and time responses. Although previous studies tell us that the wall slippage always promotes the surface flow instability of the thin film flow, the linear stability analysis, numerical simulations, and nonlinear traveling-wave solutions in the current study present a different conclusion. The analysis show that for a thin film flow with a dynamic contact line the wall slippage in different directions plays much more complex roles. The streamwise slippery effect always impedes the instability of the flow and suppresses the wave height of traveling wave, while the transverse slippery effect has a dual effect on the surface instability. The transverse slippery effect significantly improves the instability while the wave number of the perturbation is small, and simultaneously it reduces the cutoff wave number. The transverse slippery effect will change its role if the wave number of the perturbation exceeds a critical value, which can stabilize the contact line.

DOI: 10.1103/PhysRevE.101.053108

I. INTRODUCTION

Gravity-driven flows and their wide applications in engineering and biology have been hot topics for decades [1,2], and have aroused the interest of both scientists and engineers. When flowing down planes and cylinders, the interface of the film is likely to break into fingers. This kind of phenomenon is called the contact line fingering instability or capillary ridge instability [3–6].

Plenty of studies on the dynamics and linear stability analysis of the liquid coating films have been performed. For example, Miyara [7] analyzed the interfacial wave behavior of a liquid film flowing down a vertical wall and an inclined wall, and proved that a low-frequency disturbance developed to a solitary wave and the wave amplitude became small while the frequency increased. Levy *et al.* [8] studied the smooth traveling waves of a gravity-driven thin liquid film by a parameterized nonlinear partial differential equation (PDE) and analyzed the combination effect of the surface tension, the surfactant diffusivity, and the gravity-driven diffusive spreading of the fluid. Pascal and D'Alessio [9] analyzed the instability in the gravity-driven flow over uneven permeable surfaces, and a slip condition was applied, indicating that the bottom permeability destabilized the flow. Takagi and Huppert [10] investigated the dynamics of gravity-driven thin films on the outer surface of a cylinder and sphere. It was found that the thermocapillary forces or the Marangoni effect plays an important role in flow instability of thin films, and the Marangoni effect always destabilized the thin film flow [11–17]. Recently, liquid falling films on tubes attracted a lot of interest [18–23]. In general, theses studies mainly concentrated on a thin film flow without a contact line; however, the modeling method can be easily extended to fluid flow in the presence of a contact line.

For the liquid film moving over a surface, the wettability plays an important role, especially in the domain of a liquid-vapor interface meeting a solid surface. The thin film flows with contact lines have also been a popular topic for a long time, and numerical methods were usually utilized in these problems, such as finite volume method (ANSYS-FLUENT) and finite difference method. Kondic [24,25] investigated the pattern formation of thin films down an incline, and detailed implicit calculation schemes were introduced. In the studies by Warner *et al.* [26,27], direct numerical simulations were given to analyze the linear and nonlinear stability of a thin liquid film with insoluble surfactant and soluble surfactant. Lin *et al.* [28,29] simulated thin films flowing down inverted substrate, where the second-order Crank-Nicolson method in time and second-order discretization in space were implemented in two-dimensional simulations and three-dimensional simulations. Moya *et al.* [30] mainly studied fingering patterns of gravity-driven flowing films flowing outside of a cylinder, and numerical simulations were proposed by an alternating direction implicit scheme. Howell *et al.* [31] analyzed the influence of the flexible substrate on the thin film flow using numerical and perturbation methods. Hu and Sarah [32] investigated the contact line instability of power-law

*liujianlin@upc.edu.cn

fluids, and the dynamical evolution of the free interface was simulated by the finite-element method. Zheng *et al.* [33] studied the propagation of viscous gravity currents along a thin permeable substrate, and the propagating front captured from the experiments agreed well with the theoretical and numerical predictions. Yu *et al.* [34] investigated the coupled drainage mechanisms of a propagating viscous gravity current that leaked fluid through a permeable substrate. The proposed numerical methods provided practice-based reference for new problems, such as the non-Newtonian liquid and multiphase flows.

There are some general similarities in analyzing the dynamics of liquid film on porous substrates and slippery substrates, and the porous substrate is usually considered by slippery velocities. Münch and Wagner [35] investigated the linear stability of dewetting thin films and discovered that the magnitude of the contact line was larger in the slippage case than that in no-slippage case. Samanta studied gravity-driven falling film on a porous medium and a slippery inclined plane [36,37], and found nonlinear traveling waves were amplified by the presence of the slip and the slippery effect was destabilizing close to the instability onset. Ding investigated the falling films flowing down a porous vertical cylinder [38,39], obtaining a conclusion similar to that of Samanta. Liu and Ding [40] examined the effect of velocity slip on the temporal stability of a viscous film, and the destabilizing effect of velocity slip at the porous wall was concluded. Chao *et al.* [41] studied linear stability and traveling wave of thin films flowing down the nonisothermal cylinder with wall slippage, and results showed wall slippage promoted the capillary instability. The above studies mainly focus on the two-dimensional flow or isotropic slippery properties. Nowadays, inspired by the microstructures of natural animals and plants, the artificial slippery liquid-infused porous surface has been designed and reported [42–44]. Zhang *et al.* [45] designed a directional slippery liquid-infused surface in the light of immobilized lubricant menisci. Gao *et al.* [46] manipulated slippery liquid-infused porous surfaces with electric controlled reversible wettability for droplet manipulation where the local properties of the surface could be tuned by an electric field. Jiang *et al.* [47] realized the function of anisotropic slippery property, and the microdroplets could be transported directionally. Understanding the slippery effect on the thin film flow is important for the engineering application of these artificial slippery liquid-infused porous surface.

Altogether, it can be concluded from the previous studies that the slippery effect plays a destabilizing role for a thin film flowing down a plane or a cylinder. However, the influence of the slippery effect on the thin film flow with contact lines has not been investigated as yet. Therefore, the main goal of this study is directed toward a deep understanding of the slippery effect on the contact line instability of thin films flowing a vertical cylinder. The outline of the paper is organized as follows. In Sec. II, the mathematical model including the governing equation and boundary conditions is given. Next, based on the mathematical model, the time evolution of the falling film is obtained by a numerical method in Sec. III. Then in Sec. IV the traveling-wave solutions are analyzed, and in Sec. V the linear stability analysis is carried out. Finally, the paper is briefly summarized in Sec. VI.

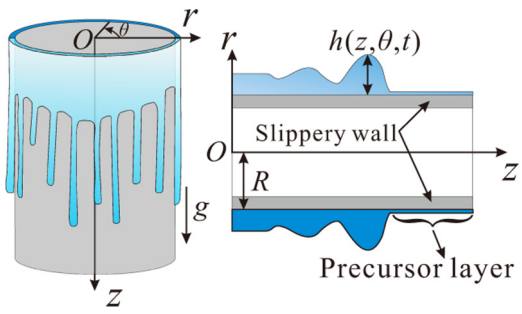

FIG. 1. Thin film flowing down the side surface of a cylinder with wall slippage, and the wall has an anisotropic slippery property.

II. GOVERNING EQUATIONS

A. Fundamental dynamic equations

In this study, we focus on the dynamic contact line of a thin film flowing down the side surface of a vertical cylinder with a slippery wall, as shown in Fig. 1. To relieve the singularity at the triple-phase contact domain, both the slip model and the precursor model are effective [5]. For the slip model, normally slip only occurs very close to the contact line. However, in this study, the slippery property is considered for the total substrate surface, and only considering the slip length close to the contact line is not enough. Hence the precursor film model is adopted to analyze the slippery effect. Using the precursor film model, it is assumed that the substrate surface is totally prewetted by a very thin fluid layer. The dynamics of the thin liquid film will be investigated, referring to the cylindrical coordinate system (r, θ, z). The radius of the cylinder is R, and the thickness of the falling film is $h(z, \theta, t)$. The fluid is considered as Newtonian and incompressible, and the symbols (u, v, w) are used to denote the velocities related to the coordinates (r, θ, z), respectively. The dynamic viscosity and the density of the fluid are represented by μ and ρ, respectively, and the gravitational acceleration is denoted by g. The motion of the thin film flow is described by the continuity equation and the Navier-Stokes equations in the cylindrical coordinate:

$$\frac{1}{r}\frac{\partial(ru)}{\partial r} + \frac{1}{r}\frac{\partial v}{\partial \theta} + \frac{\partial w}{\partial z} = 0, \tag{1}$$

$$\rho\left(\frac{Du}{Dt} - \frac{v^2}{r}\right) = -\frac{\partial p}{\partial r} + \mu\left(\Im u - \frac{u}{r^2} - \frac{2}{r^2}\frac{\partial v}{\partial \theta}\right), \tag{2}$$

$$\rho\left(\frac{Du}{Dt} + \frac{uv}{r}\right) = -\frac{1}{r}\frac{\partial p}{\partial \theta} + \mu\left(\Im v - \frac{v}{r^2} + \frac{2}{r^2}\frac{\partial u}{\partial \theta}\right), \tag{3}$$

$$\rho\frac{Du}{Dt} = -\frac{\partial p}{\partial z} + \mu\Im v + \rho g, \tag{4}$$

where p is the pressure and the operator D/Dt represents the material derivative:

$$\frac{D}{Dt} = \frac{\partial}{\partial t} + u\frac{\partial}{\partial r} + \frac{v}{r}\frac{\partial}{\partial \theta} + w\frac{\partial}{\partial z}. \tag{5}$$

The symbol $\Im$ is a simple operator with the following expression:

$$\Im = \frac{\partial^2}{\partial r^2} + \frac{1}{r}\frac{\partial}{\partial r} + \frac{1}{r^2}\frac{\partial^2}{\partial \theta^2} + \frac{\partial^2}{\partial z^2}. \tag{6}$$

To derive the equivalent model for the thin film flow, the following scalings are to be applied [24]:

$$(u', v', w') = \left(\frac{u}{\epsilon W}, \frac{v}{W}, \frac{w}{W}\right), \quad (r', z') = \left(\frac{r}{L}, \frac{z}{L}\right), \quad (p', t') = \left(\frac{p}{P}, \frac{t}{T}\right), \tag{7}$$

where the symbols with primes represent nondimensional parameters. Using a representative height scale h_0 for the thickness of the film and a representative length scale L in the z and azimuthal directions, the characteristic velocity, pressure, length, and timescales are rescaled as [24,30]

$$W = \frac{\rho g h_0^2}{3\mu}, \quad P = \frac{\rho g L}{3}, \quad L = \left(\frac{\sigma h_0}{\rho g}\right)^{\frac{1}{3}}, \quad T = \frac{L}{W}. \tag{8}$$

Considering that the thickness of the liquid film is much smaller compared to the wavelength of the interfacial waves, a small parameter $\epsilon = h_0/L$ is introduced to rescale the radial coordinate. The scaled radial coordinate is rewritten as $r' = R' + \epsilon x'$, where $R' = R/L$ and $x' = x/h_0$. After rescaling Eqs. (1)–(4) and dropping the primes for simplicity, the resulting nondimensional equations give

$$\frac{1}{r}\frac{\partial (ru)}{\epsilon \partial x} + \frac{1}{r}\frac{\partial v}{\partial \theta} + \frac{\partial w}{\partial z} = 0, \tag{9}$$

$$\epsilon^4 \mathrm{Re}\left(\frac{Du}{Dt} - \frac{1}{\epsilon}\frac{v^2}{r}\right) = -\frac{\partial p}{\partial x} + \epsilon^4\left(\Im u - \frac{u}{r^2} - \frac{1}{\epsilon}\frac{2}{r^2}\frac{\partial v}{\partial \theta}\right), \tag{10}$$

$$\epsilon^2 \mathrm{Re}\left(\frac{Du}{Dt} - \epsilon\frac{uv}{r}\right) = -\frac{1}{r}\frac{\partial p}{\partial \theta} + \epsilon^2\left(\Im v - \frac{v}{r^2} + \epsilon\frac{2}{r^2}\frac{\partial u}{\partial \theta}\right), \tag{11}$$

$$\epsilon^2 \mathrm{Re}\frac{Dw}{Dt} = -\frac{\partial p}{\partial z} + \epsilon^2 \Im w + 3, \tag{12}$$

where $\mathrm{Re} = \rho W L/\mu$ denotes the Reynolds number.

Using the scaling, the operators D/Dt and $\Im$ become

$$\frac{D}{Dt} = \frac{\partial}{\partial t} + u\frac{\partial}{\partial x} + \frac{v}{r}\frac{\partial}{\partial \theta} + w\frac{\partial}{\partial z}, \tag{13}$$

$$\Im = \frac{1}{\epsilon^2}\frac{\partial^2}{\partial x^2} + \frac{1}{r}\frac{\partial}{\epsilon \partial x} + \frac{1}{r^2}\frac{\partial^2}{\partial \theta^2} + \frac{\partial^2}{\partial z^2}. \tag{14}$$

B. Boundary conditions

On the side of the cylinder $r = R$, the no-slip and no-penetration conditions are applied in the r direction, while the Navier slip boundary conditions are applied in θ and z directions to describe the slippery property [39–41]:

$$u = 0, \quad v = \beta_1 \frac{\partial v}{\partial r}, \quad w = \beta_2 \frac{\partial w}{\partial r}. \tag{15}$$

The Navier slip boundary condition is defined by a slip velocity proportional to the shear stress, and parameters β_1 and β_2 are used to characterize the slip length in θ direction and z direction, respectively. For a standard no-slip condition, one can let $\beta_i = 0$. On the surface $r = R + h$, the normal stress balance and tangential stress balance are satisfied [38,40]:

$$(\boldsymbol{T} - \boldsymbol{T}_\infty)\cdot \boldsymbol{n} = -\nabla_s \sigma + \sigma(\nabla \cdot \boldsymbol{n})\boldsymbol{n}, \tag{16}$$

where $\boldsymbol{T} = \mu[\nabla \boldsymbol{u} + \nabla \boldsymbol{u}^T]$ is the deviatoric stress tensor, and $\boldsymbol{T}_\infty = (p - p_\infty)\boldsymbol{I}$ is the pressure tensor. The symbol p_∞ is the pressure of the surrounding gas phase, and $\nabla_s = \nabla - \boldsymbol{n}(\boldsymbol{n}\cdot\nabla)$ stands for the surface gradient operator, and $\boldsymbol{n}$ is the unit vector normal to the liquid surface.

The kinematic condition of the interface should be satisfied at $x = h$ $(r = R + h)$, expressed by the mass conservative condition

$$\frac{\partial h}{\partial t} + \frac{1}{R}\frac{\partial}{\partial \theta}\int_0^h v dx + \frac{\partial}{\partial z}\int_0^h w dx = 0. \tag{17}$$

Using the scalings introduced in Eq. (7), the boundary conditions at $x = 0$ $(r = R)$ become

$$u = 0, \quad v = \beta_\theta \frac{\partial v}{\partial x}, \quad w = \beta_z \frac{\partial w}{\partial x}. \tag{18}$$

The coefficients which occur in the boundary conditions are the scaled slippery lengths $\beta'_\theta = \epsilon^{-1}\beta_\theta/h_0$ and $\beta'_z = \epsilon^{-1}\beta_z/h_0$ [41]. Here the primes are also dropped for simplicity.

Neglecting the terms of $O(\epsilon)$ and higher orders, the normal stress balance becomes [30]

$$p_0 = \frac{3}{\epsilon R} - \frac{3h}{R^2} - \frac{3}{R^2}\frac{\partial^2 h}{\partial \theta^2} - 3\frac{\partial^2 h}{\partial z^2}, \tag{19}$$

where the variables with subscript 0 represent the leading-order components.

The boundary conditions for the tangential stress balance on the free interface $x = h$ $(r = R + h)$ are reduced as [30]

$$\frac{\partial v_0}{\partial x} + O(\epsilon) = 0, \quad \frac{\partial w_0}{\partial x} + O(\epsilon) = 0. \tag{20}$$

The kinematic condition of the interface is still of the same form as Eq. (17):

$$\frac{\partial h}{\partial t} + \frac{1}{R}\frac{\partial}{\partial \theta}\int_0^h v dx + \frac{\partial}{\partial z}\int_0^h w dx = 0. \tag{21}$$

C. Governing equations

As $\epsilon \ll 1$ and $\mathrm{Re} \sim O(1)$ [40], the contributions of the inertial terms are neglected. Ignoring the terms of the second and higher orders of the small parameter ϵ, the continuity equation (9) and Navier-Stokes equations (10)–(12) are given as

$$\frac{\partial u_0}{\partial x} + \frac{1}{R}\frac{\partial v_0}{\partial \theta} + \frac{\partial w_0}{\partial z} = 0, \tag{22}$$

$$\frac{\partial p_0}{\partial x} = 0, \tag{23}$$

$$\frac{\partial^2 v_0}{\partial x^2} = \frac{1}{R}\frac{\partial p_0}{\partial \theta}, \tag{24}$$

$$\frac{\partial^2 w_0}{\partial x^2} = \frac{\partial p_0}{\partial z} - 3. \tag{25}$$

Solving Eqs. (24) and (25) and using the boundary conditions in Eqs. (18) and (20), the velocities of the leading order

are expressed as

$$w_0 = \frac{1}{2}\left(\frac{\partial p_0}{\partial z} - 3\right)(x^2 - 2hx - 2\beta_z h), \tag{26}$$

$$v_0 = \frac{1}{2}\frac{\partial p_0}{\partial \theta}(x^2 - 2hx - 2\beta_\theta h). \tag{27}$$

Substituting w_0 and v_0 into the kinematic condition (21), and using the normal balance condition (19), the governing equation for the thin film flowing on a cylinder with wall slippage is derived as

$$h_t + (h^3 + 3\beta_z h^2)_z + \nabla \cdot \left[\mathfrak{R}\nabla\left(\nabla^2 h + \frac{h}{R^2}\right)\right] = 0, \tag{28}$$

where $\nabla = (\frac{1}{R}\partial_\theta, \partial_z)$ and $\mathfrak{R}$ is a coefficient matrix:

$$\mathfrak{R} = \begin{bmatrix} \Re(\theta) & 0 \\ 0 & \Re(z) \end{bmatrix} = \begin{bmatrix} h^3 + 3\beta_\theta h^2 & 0 \\ 0 & h^3 + 3\beta_z h^2 \end{bmatrix}. \tag{29}$$

If we only consider the two-dimensional flow in the r-z plane, Eq. (28) is identical with Eq. (30) derived by Chao [41]. For $\beta_\theta = 0$ and $\beta_z = 0$, Eq. (28) degenerates into the equation obtained by Moya [30]. Notably, the surface instability is influenced by the coupling action of the slippery length, the substrate curvature, and the initial condition consisting of a randomly perturbed contact line. Therefore, in the following sections, a systematic analysis of the interfacial characteristics affected by the multiparameter is developed by numerical simulations and linear stability analysis.

III. TIME EVOLUTIONS

To solve the high-order partial differential equation (PDE) (28), the finite difference method (FDM) and finite element method (FEM) are both efficient and accurate. Here the open-source software FREEFEM++ is used to solve the governing equation based on the FEM [48]. As the PDE (28) is spatial fourth order, four boundary conditions should be prescribed in the z as well as in the θ directions. In this problem, it is assumed the thickness of the liquid film is constant both far behind and far in front of the initial contact line. Therefore, the following boundary conditions are applied in the z direction [25,28,29]:

$$\begin{aligned} h(0,\theta,t) &= 1, \quad h(L_z,\theta,t) = b, \\ h_z(0,\theta,t) &= 0, \quad h_z(L_z,\theta,t) = 0, \end{aligned} \tag{30}$$

where L_z is the length of the calculation domain in the z direction, and b is the thickness of the precursor layer. In the θ direction, a periodic boundary condition (PBC) is applied. Different initial conditions can be chosen for this problem [6,25,29,32]. In fact, these functions are very similar; i.e., all the profiles are two flat regions connected via a transitional part. It has been illustrated that the influence of the initial condition on the final results is insignificant. The following initial condition is adopted in this paper for its brevity [29]:

$$h_{t0} = \frac{1+b}{2} - \frac{1-b}{2}\tanh(x - x_p), \tag{31}$$

where x_p marks the position of the front of the initial contact line.

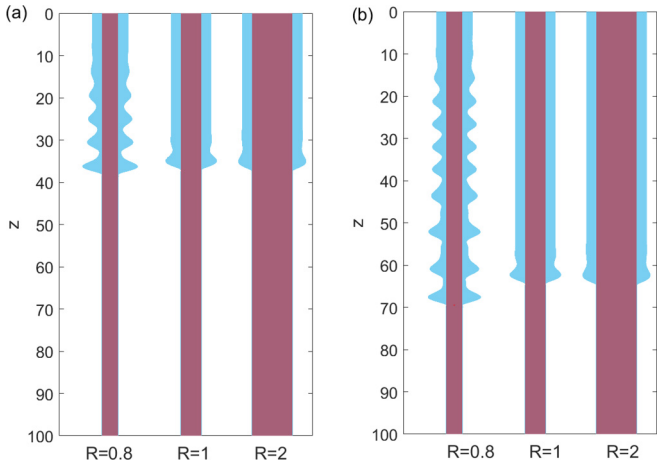

FIG. 2. Asymmetric flow profiles of thin liquid films on vertical cylinders for (a) $t = 20$, $R = [0.8, 1, 2]$, and (b) $t = 40$, $R = [0.8, 1, 2]$. The used parameters are $\beta_z = 0.1$, $\beta_\theta = 0$, and $b = 0.05$.

Using FREEFEM++ [14,49], the governing equation (28) is numerically solved. A linearization of the system is first proposed by the estimation $h_{t+\Delta t} = h_t + \Delta h$. Then the Crank-Nicolson method is employed to average the results from the current and future times, obtaining a better estimation of the time evolution. In the simulation, asymmetric profiles are obtained, which are plotted in a r-z plane.

First, the influence of the substrate curvature is investigated. Three radii for the cylinder are used in the simulations, including $R = 0.8$, $R = 1$, and $R = 2$. Figure 2 shows the three-dimensional shapes of the liquid thin film at the instant $t = 20$ and $t = 40$ for various substrate curvatures. While the cylinder has a small radius, the interface becomes very complex after a while. At $t = 20$, a wave train is found following the capillary ridge. At $t = 40$, besides the capillary ridge and a wave train, solitary-type waves appear at the middle of the wave train and the capillary ridge. With a smaller radius, such as the case for a fiber, the Rayleigh-Plateau instability occurs, and a beading phenomenon will be observed. We can note that the characteristic height of a hump is much smaller compared to the distance between the two humps. For $R = 1$ and larger value of R, the liquid-air interface keeps a dominant capillary ridge, and the substrate curvature does not affect the traveling velocity of the capillary bump. From the profiles, it is seen that the capillary ridge for $R = 0.8$ goes longer than that for $R = 1$ and $R = 2$. The reason is that the waves behind the capillary ridge move faster than the front [28], and hence the first wave will catch up, interact, and merge with the capillary ridge, speeding up and raising the ridge.

In view of the characteristic lengths of the film thickness and the largest slip length, $\beta_{z,\theta} \in [0, 0.2]$ is reasonable [41], and the slippery effect can be stronger for some biomaterials and compliant substrates. Using different slippery lengths and precursor layer thicknesses, the evolution profiles of liquid films at $t = 20$ and $t = 40$ are displayed in Figs. 3 and 4, respectively. The interfacial shapes show similar patterns and traveling wave trends: A dominant capillary ridge travels more quickly with a larger β_z or b, and behind the main ridge is a weak wave and a constant state. Measurement of the capillary ridge shows that the height of the main ridge becomes lower

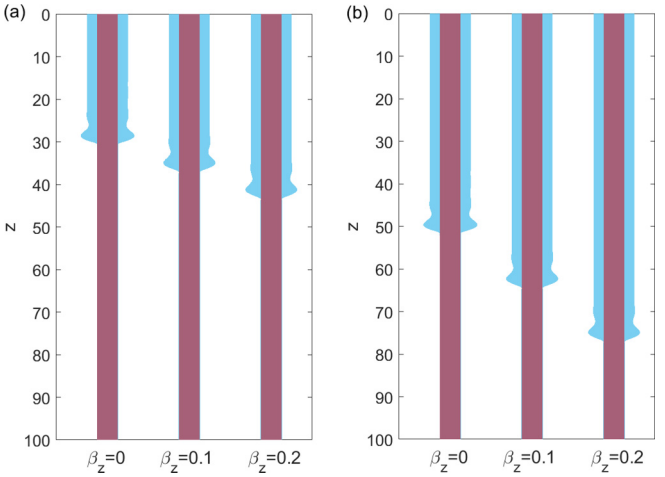

FIG. 3. Asymmetric flow profiles of thin liquid films on vertical cylinders for (a) $t = 20$, $\beta_z = [0, 0.1, 0.2]$, and (b) $t = 40$, $\beta_z = [0, 0.1, 0.2]$. The used parameters are $b = 0.05$, $\beta_\theta = 0$, and $R = 1$.

while the value of β_z or b is larger. The evolution of small disturbances applied on the steady traveling waves is very crucial to understanding the hydrostability of thin liquid films. Therefore, in next section, the behavior of steady traveling waves is investigated.

IV. TRAVELING-WAVE SOLUTIONS

From the numerical simulation, the asymmetric traveling wave profiles are obtained. The two-dimensional asymmetric flows play important roles in understanding the flow instability. Here we neglect the fingering patterns in advance and assume θ is independent of the evolution equation. Hence the evolution equation (28) is simplified as

$$h_t + \frac{\partial}{\partial z}\left[(h^3 + \beta_z h^2)\left(1 + h_{zzz} + \frac{h_z}{R^2}\right)\right] = 0. \qquad (32)$$

Equation (32) is solved by the FEM as well, and the profiles for different cases are displayed in Figs. 5–7. Comparing

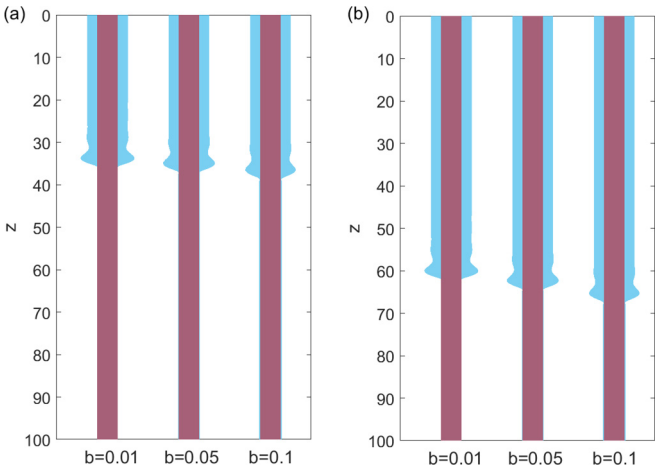

FIG. 4. Asymmetric flow profiles of thin liquid films on vertical cylinders considering different precursor thickness: (a) $t = 20$, $b = [0.01, 0.05, 0.1]$, and (b) $t = 40$, $b = [0.01, 0.05, 0.1]$. The used parameters are $\beta_z = 0.1$, $\beta_\theta = 0$, and $R = 1$.

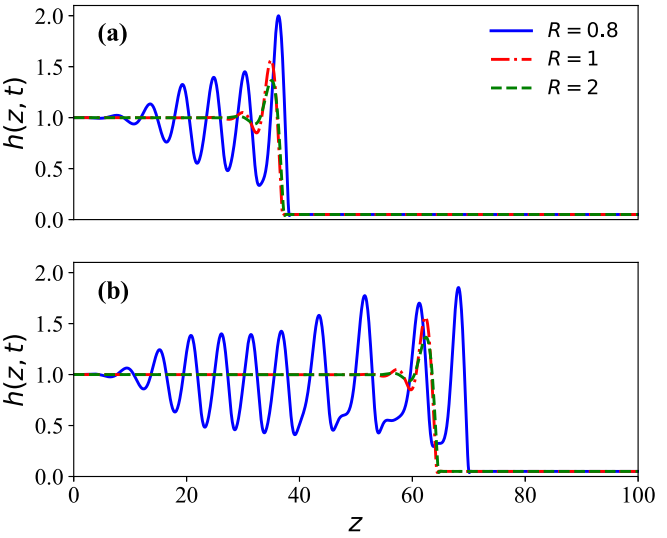

FIG. 5. The evolution profiles of the liquid-air interface for different substrate curvature at (a) $t = 20$ and (b) $t = 40$, including $R = 0.8$ (solid line), $R = 1$ (dash-dotted line), and $R = 2$ (dashed line).

the curves in Figs. 5–7 and those in Figs. 2–4, it is notable that the two-dimensional profiles and the three-dimensional profiles are exactly consistent. For the different radii of the cylinder, the substrate curvature significantly affects the axial waves along the free surface, especially when the cylinder has a much smaller radius, as shown in Fig. 5. It is displayed in Figs. 6 and 7 that with a bigger b and β_z, the contact lines move faster and have a lower capillary ridge. This phenomenon is contrary to the results of Ding [38,39] and Chao [41], as they found that the wall slippage amplified the capillary ridge. The main reason is that for thin film flows without contact lines, the slippery effect promotes the propagation of the nonlinear waves and causes a steeper wave.

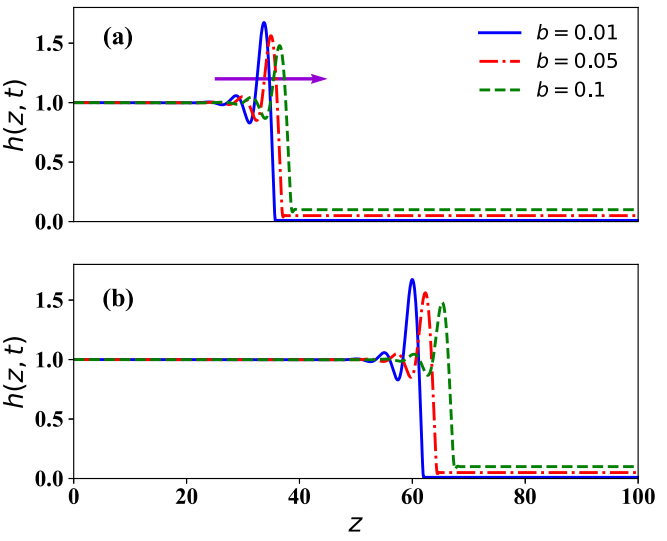

FIG. 6. The evolution profiles of the liquid-air interface considering different precursor thickness at (a) $t = 20$ and (b) $t = 40$, including $b = 0.01$ (solid line), $b = 0.05$ (dash-dotted line), and $b = 0.1$ (dashed line).

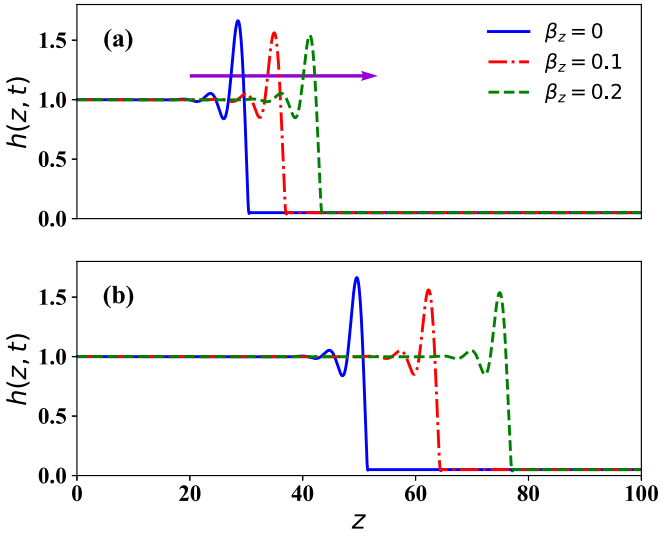

FIG. 7. The evolution profiles of the liquid-air interface on the cylinders with different slippery lengths at (a) $t = 20$ and (b) $t = 40$, including $\beta_z = 0$ (solid line), $\beta_z = 0.1$ (dash-dotted line), and $\beta_z = 0.2$ (dashed line).

While for thin film flows with dynamic contact lines, the slippery effect increases the traveling speed of the front of the contact lines, resulting in a significant drop of the capillary ridge. From the curves in Fig. 7, the traveling wave speed can

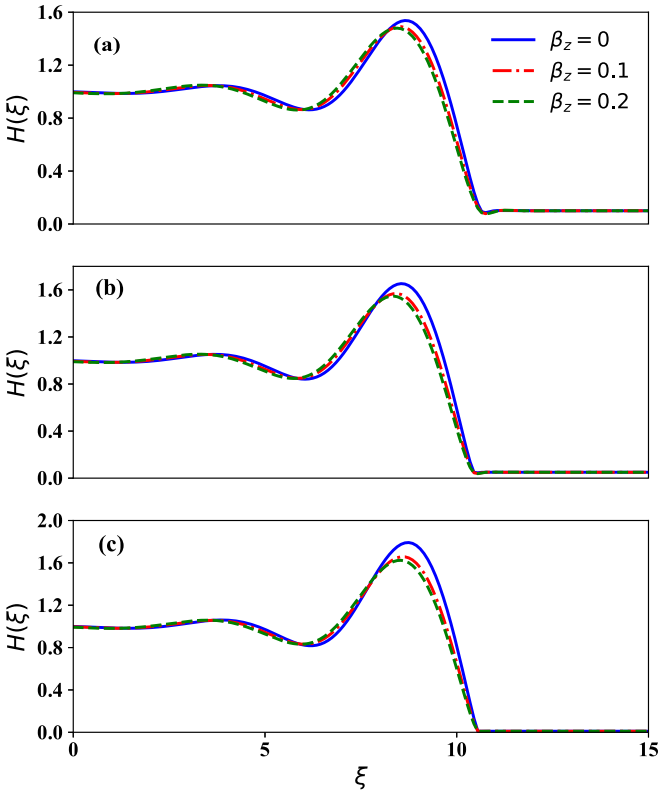

FIG. 8. Traveling-wave profiles of the liquid-air interface for $\beta_z = 0$ (solid line), $\beta_z = 0.1$ (dash-dotted line), and $\beta_z = 0.2$ (dashed line): (a) $b = 0.1$ corresponding to different β_z, (b) $b = 0.05$ corresponding to different β_z, and (c) $b = 0.01$ corresponding to different β_z.

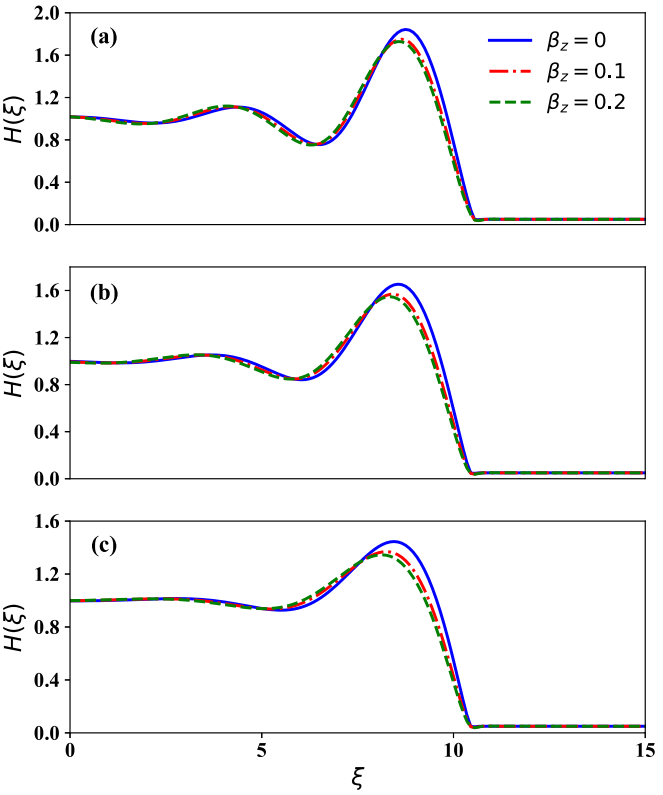

FIG. 9. Traveling-wave profiles of the liquid-air interface for $\beta_z = 0$ (solid line), $\beta_z = 0.1$ (dash-dotted line), and $\beta_z = 0.2$ (dashed line): (a) $R = 0.8$ corresponding to different β_z, (b) $R = 1$ corresponding to different β_z, and (c) $R = 2$ corresponding to different β_z.

be calculated by the distance between the two ridges, and for $\beta_z = 0$, $\beta_z = 0.1$, and $\beta_z = 0.2$, the speed is 1.315, 1.37, and 1.44, respectively.

It has been found from the numerical simulations that the falling film exhibits a traveling-wave solution [24,25], and hence a coordinate transformation $\xi = z - ct$ is helpful and effective to understand the nonlinear flow characteristics, where c represents the traveling-wave speed. In this study, the symbol H is used for the coordinate ξ while h is used for the coordinate z. Using the transformation $\xi = z - ct$, Eq. (32) changes to an ordinary differential equation of coordinate ξ:

$$cH_\xi = (H^3 + 3\beta_z H^2)_\xi + \left[\Re(z)\left(H_{\xi\xi\xi} + \frac{1}{R^2}H_\xi\right)\right]_\xi. \quad (33)$$

Integrating Eq. (33) once, we can obtain the following equation:

$$cH = H^3 + 3\beta_z H^2 + \Re(z)\left(H_{\xi\xi\xi} + \frac{1}{R^2}H_\xi\right) + d, \quad (34)$$

where d is an integral constant.

Based on the boundary conditions [in Eq. (30)], the traveling speed and the integral constant can be obtained as $c = (1 + b + b^2) + 3\beta_z(1 + b)$ and $d = -b(1 + b) - 3\beta_z b$. The traveling wave speed is related to the combined action of the streamwise slippery length and the thickness of the precursor layer. Both the streamwise slippery length and the thickness of the precursor layer speed up the motion of the film front.

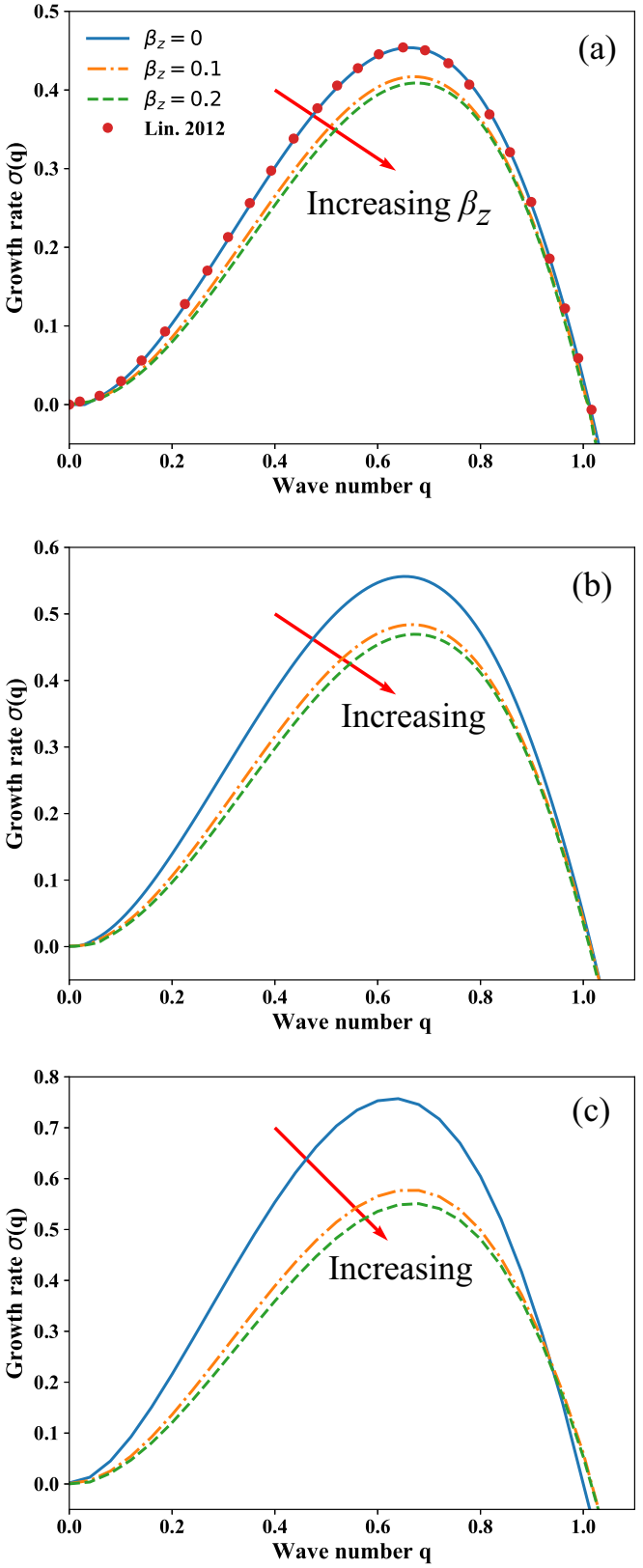

FIG. 10. Temporal growth rate $\sigma(q)$ vs wave number q for $\beta_z = 0$ (solid line), $\beta_z = 0.1$ (dash-dotted line), and $\beta_z = 0.2$ (dashed line): (a) $b = 0.1$, (b) $b = 0.05$, and (c) $b = 0.01$. Red circle shows the prediction in the previous study by Lin [29]. Arrow represents the increase of the streamwise slippery effect.

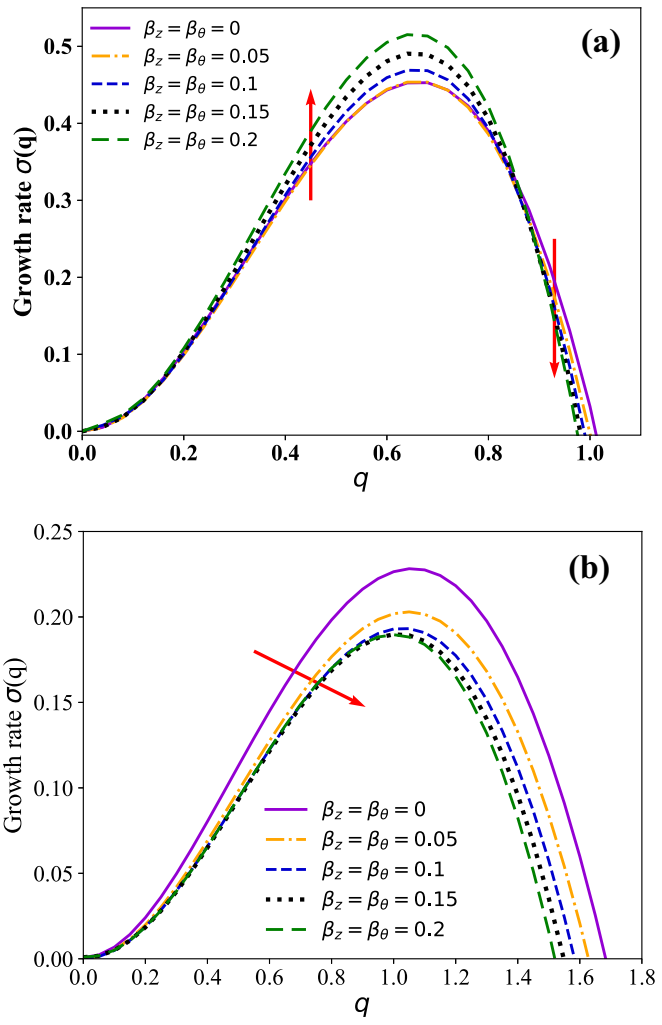

FIG. 11. Temporal growth rate $\sigma(q)$ versus wave number q for (a) $R = 1$ and (b) $R = 2$. Arrow represents the increase of the slippery effect.

Compared with the conclusion of Chao [41], the traveling speed of the thin film flow with dynamic contact lines is equal to that without dynamic contact lines. With $b = 0.05$, using the function of c, the traveling speeds are 1.3131, 1.3675, and 1.4400, respectively for $\beta_z = 0$, $\beta_z = 0.1$, and $\beta_z = 0.2$, showing good consistency with the numerical simulations.

Given c and d, traveling-wave shapes can be depicted by solving Eq. (34). Here, Eq. (34) is numerically solved using the Newton's iteration method, with the central difference formulas employed to discretize the spatial domain. The initial condition is also given by a smooth curve of two flat regions connected via a transitional part [28,29]:

$$H_o = \frac{1+b}{2} - \frac{1-b}{2}\tanh(\xi - \xi_p), \tag{35}$$

where ξ_p is also a parameter marking the position of the front of the initial contact line.

Figure 8 gives traveling-wave profiles for different precursor film thickness b and slippery length β_z. It is noticed that with a smaller value of b from Figs. 8(a) to 8(c), the height

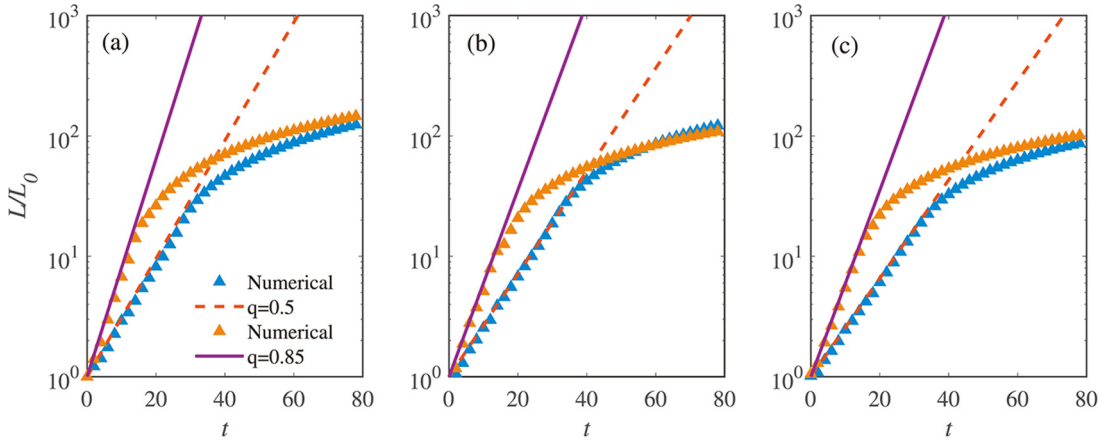

FIG. 12. Comparison of growth rates between LSA ($q = 0.85$ [solid lines] and $q = 0.5$ [dashed lines]) and numerical simulations (triangle markers): (a) $\beta_z = \beta_\theta = 0$, (b) $\beta_z = \beta_\theta = 0.1$, and (c) $\beta_z = \beta_\theta = 0.2$.

of the capillary ridge becomes steeper, demonstrating that the thin film flow is opt to become unstable with a smaller precursor film thickness. The main reason is that thinner films experience much more resistance than thicker films, resulting in a steeper fluid bump. The solid line shows that the traveling-wave profile for $\beta_z = 0$ has a steeper capillary ridge. With a larger $\beta_z = 0.1$ (dash-dotted line) and $\beta_z = 0.2$ (dashed line), the height of the capillary ridge becomes smaller, illustrating that the slippery length also plays a stabilizing role. The conclusion is opposite to that obtained in the study of falling films without dynamic contact lines [38,39,41]. The main reason is that the slippery length promotes the traveling wave while the volume flow rate is constant, and therefore the height of the capillary ridge reduces.

Figure 9 displays the traveling-wave profiles for film flows down cylinders of different radii. The numerical simulations and the traveling-wave profiles illustrate that increasing substrate curvature greatly increases the strength of fingering instability at the contact lines, characterized by a higher capillary ridge. For thin films flowing down a much longer and slender cylinder, one can refer to the studies on thin films flowing down a fiber [50,51]. In the following analysis, $R \geqslant 1$ will be employed, and linear stability analysis will be given based on the traveling-wave solutions.

V. LINEAR STABILITY ANALYSIS

Experiments show that the contact line develops an undulatory pattern in θ direction that grows into a fingering pattern [30]. Here the stability of the axisymmetric traveling waves with the moving frame $(\xi, \theta) = (z - ct, \theta)$ is investigated. Using the moving frame, Eq. (28) changes to

$$H_t - cH_\xi + (H^3 + 3\beta_z H^2)_\xi + \nabla \cdot \left[\mathfrak{R} \nabla \left(\nabla^2 H + \frac{H}{R^2} \right) \right] = 0 . \tag{36}$$

To conduct a linear stability analysis (LSA), the traveling-wave solutions obtained by Eq. (34) are used as basic states. Giving a perturbation in the azimuthal direction to the traveling-wave basic state, we have $H = \bar{H} + H'(t, \xi, \theta)$, and then the linear stability analysis is performed by studying the evolution of the perturbation. Substituting H into Eq. (36), a linearized simplification of the governing equation is deduced as

$$\begin{aligned} &\frac{\partial H'}{\partial t} - c\frac{\partial H'}{\partial \xi} + \frac{\partial}{\partial \xi}(3\bar{H}^2 H' + 6\beta_z \bar{H} H') \\ &\quad + \frac{\partial}{\partial \xi}\left[\mathfrak{R}(z) \frac{\partial}{\partial \xi}\left(\frac{H'}{R^2} + \nabla^2 H' \right) \right] \\ &\quad + \frac{\partial}{\partial \xi}\left[(3\bar{H}^2 H' + 6\beta_z \bar{H} H') \frac{\partial}{\partial \xi}\left(\frac{\bar{H}}{R^2} + \nabla^2 \bar{H} \right) \right] \\ &\quad + \frac{1}{R}\frac{\partial}{\partial \theta}\left[\mathfrak{R}(\theta) \frac{1}{R}\frac{\partial}{\partial \theta}\left(\frac{H'}{R^2} + \nabla^2 H' \right) \right] = 0. \end{aligned} \tag{37}$$

For each wave number q, Eq. (37) can be formulated as a standard eigenvalue equation:

$$\sigma \hat{H} = -\boldsymbol{L}\hat{H}, \tag{38}$$

where $\boldsymbol{L}$ is a linear operator. Equation (38) is solved numerically to obtain the values of $\sigma(q)$ for different wave number q, following the work by Kondic [25].

Figure 10 shows the temporal growth rate of disturbance with different β_z for given b, and the transverse slippery length β_θ is neglected. For $b = 0.1$ and $\beta_z = 0$, no slippery effect acts in the thin film flow, and the LSA result is consistent with that in the previous study [29]. Seen from these three figures that with a smaller thickness of precursor layer b, the value of the growth rate for a given q becomes larger, demonstrating that the thickness of the precursor stabilizes the thin film flow. Based on the three cases for b, one can find that with a small thickness of precursor layer b, the influence of the slippery length is enhanced. From the comparison of the growth rate curves with different slippery length β_z, it can be concluded that the slippery effect also plays a stabilizing role on the film flow. The main reason is that the slippery speeds up the flow of the contact line and reduces the height of the fluid bump, and hence the instability of the flow is suppressed. But for the thin film flowing without contact line, the slippery effect always destabilizes the flow [38,39,41], and a larger slippery length results in a steeper wave with a higher hump.

Figure 11 shows the temporal growth rate of disturbance for two different R. The isotropic slippery property is taken

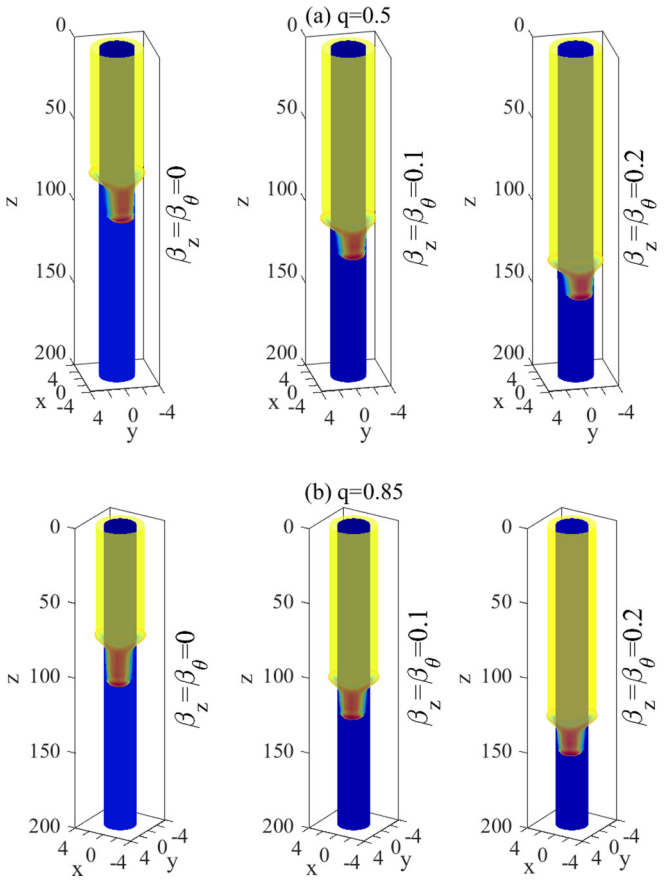

FIG. 13. Three-dimensional illustrations of a single-mode perturbed fluid film flowing on the surface of a vertical cylinder: (a) $q = 0.5$, $\beta_{z,\theta} = [0, 0.1, 0.2]$, and (b) $q = 0.85$, $\beta_{z,\theta} = [0, 0.1, 0.2]$. The radius of the cylinder is $R = 2$.

into consideration, meaning that the transverse slippery length β_θ is equal to the streamwise slippery length. For $R = 1$, the slippery length plays a destabilizing role or a stabilizing role, owing to the value of the wave number. While the wave number is small, the slippery length destabilizes the surface flow, but if the wave number exceeds a special value, the role of slippery length changes to stabilizing the flow. For $R = 2$, it can be found that the slippery effect always plays a stabilizing role in the contact line instability, implying that the substrate curvature also affects the surface stability significantly.

Figure 12 shows the comparison of the growth rate of a finger from numerical simulations and from LSA results. In the figures, L represents the total length of a finger from the top to the root, and L_0 is the initial length. The numerical results are a bit smaller than the numerical simulations, and the difference may be caused by the inaccurate measurement resulting from the coarse mesh grid. The linear growth is found at the earlier times, and then the length of the fingers grows at a smaller rate. This behavior appears to result from the local action of the front domain, where the surface tension affects the other part of the finger negligibly.

The three-dimensional illustrations of a single-mode perturbed film flow are displayed in Fig. 13. The dimensionless radius of the cylinder is set to $R = 2$, and $q = 0.5$ and $q = 0.85$ are utilized, respectively plotted in Figs. 13(a) and 13(b).

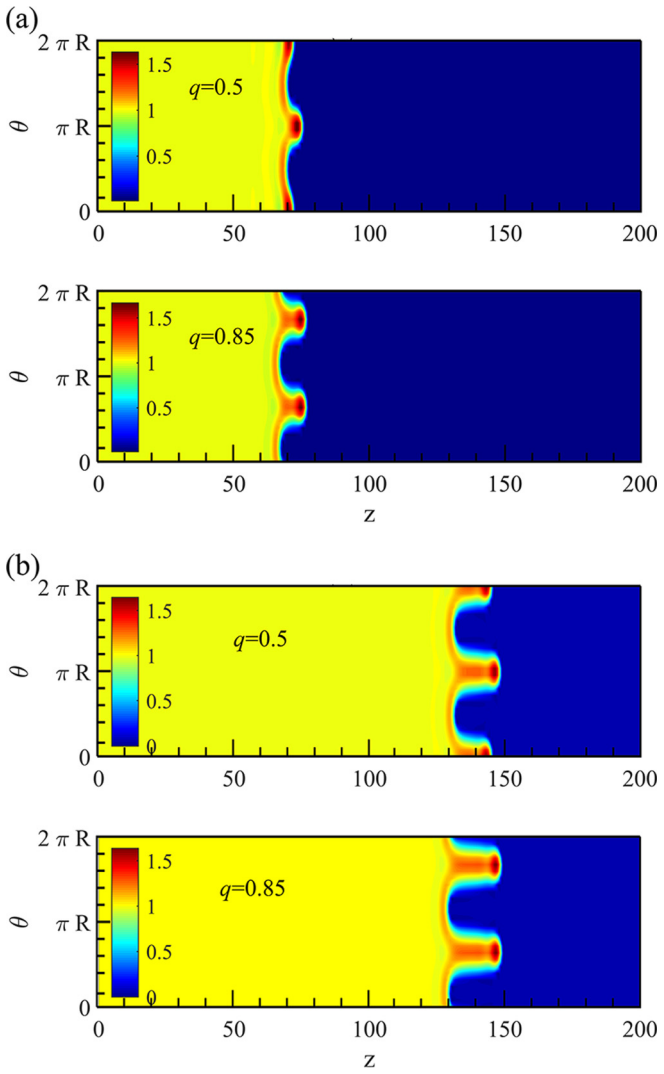

FIG. 14. Time evolution of a single-mode perturbed fluid film plotted in the Cartesian coordinate: (a) $t = 40$, $\beta_{z,\theta} = 0.2$, $R = 2$, and (b) $t = 80$, $\beta_{z,\theta} = 0.2$, $R = 2$.

The total length of a finger is measured from the top to the root. From the figures, it can be found for a larger slippery length, the contact lines move faster. To show the results more distinctly, one can replot the results in the Cartesian coordinate, as displayed in Fig. 14, where $\beta_z = \beta_\theta = 0.2$ and $R = 2$. The time evolutions for $t = 40$ and $t = 80$ are both visualized. The length displayed in the lower plots is much longer than that shown in the upper plots, showing an agreement with the linear stability analysis that the growth rate for $q = 0.85$ is bigger than that for $q = 0.5$. From Fig. 14(b), it is also found that the difference between the length for $q = 0.5$ and that for $q = 0.85$ is little, consistent with the LSA that the growth rates are close after a long time evolution.

In the above analysis, isotropic slippery property is taken into account, as a result, it is hard to distinguish the direct influence of the two slippery lengths. Here anisotropic slippery property is also considered, and different transverse slippery lengths are examined while the streamwise slippery length is given a specific value. Linear stability analysis is carried out, and the temporal growth rates for different azimuthal slippery

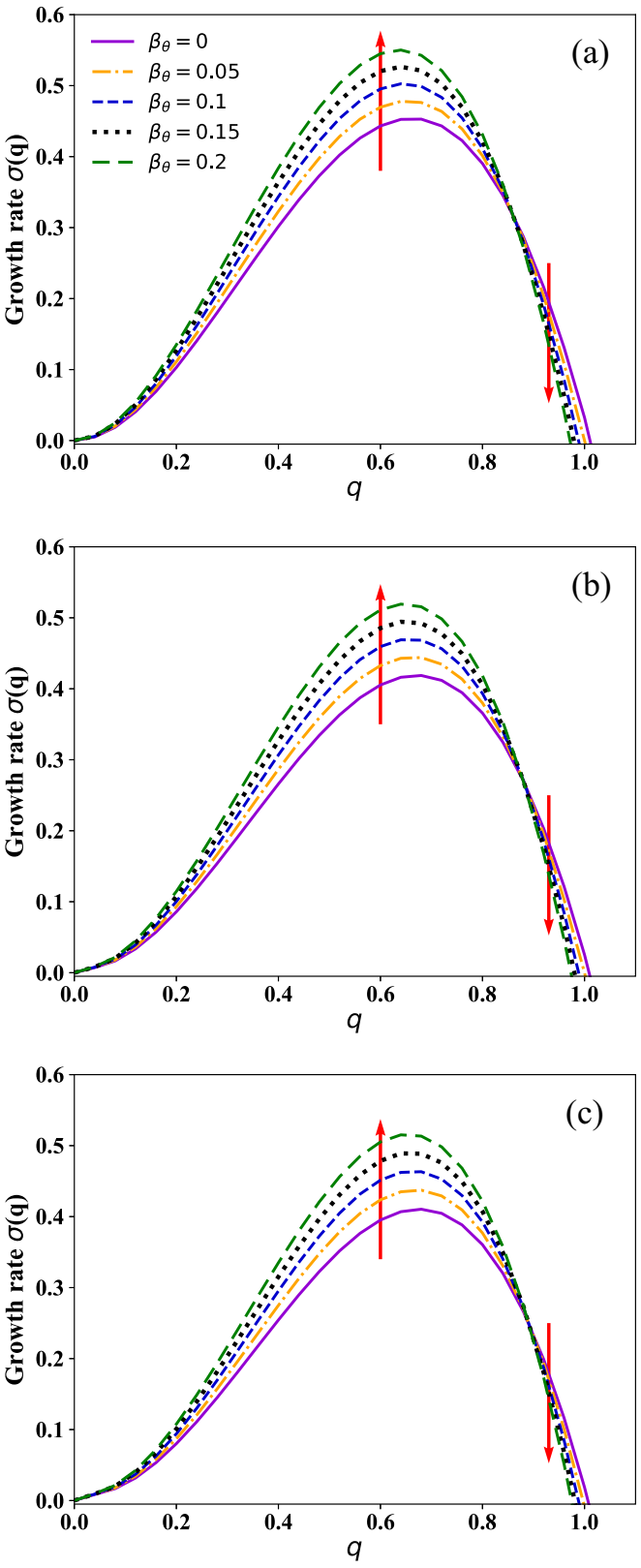

FIG. 15. Temporal growth rate $\sigma(q)$ vs wave number q for different azimuthal slippery lengths: (a) $\beta_z = 0$, (b) $\beta_z = 0.1$, and (c) $\beta_z = 0.2$. Arrow represents the increase of the azimuthal slippery effect, $\beta_\theta = [0, 0.05, 0.1, 0.15, 0.2]$.

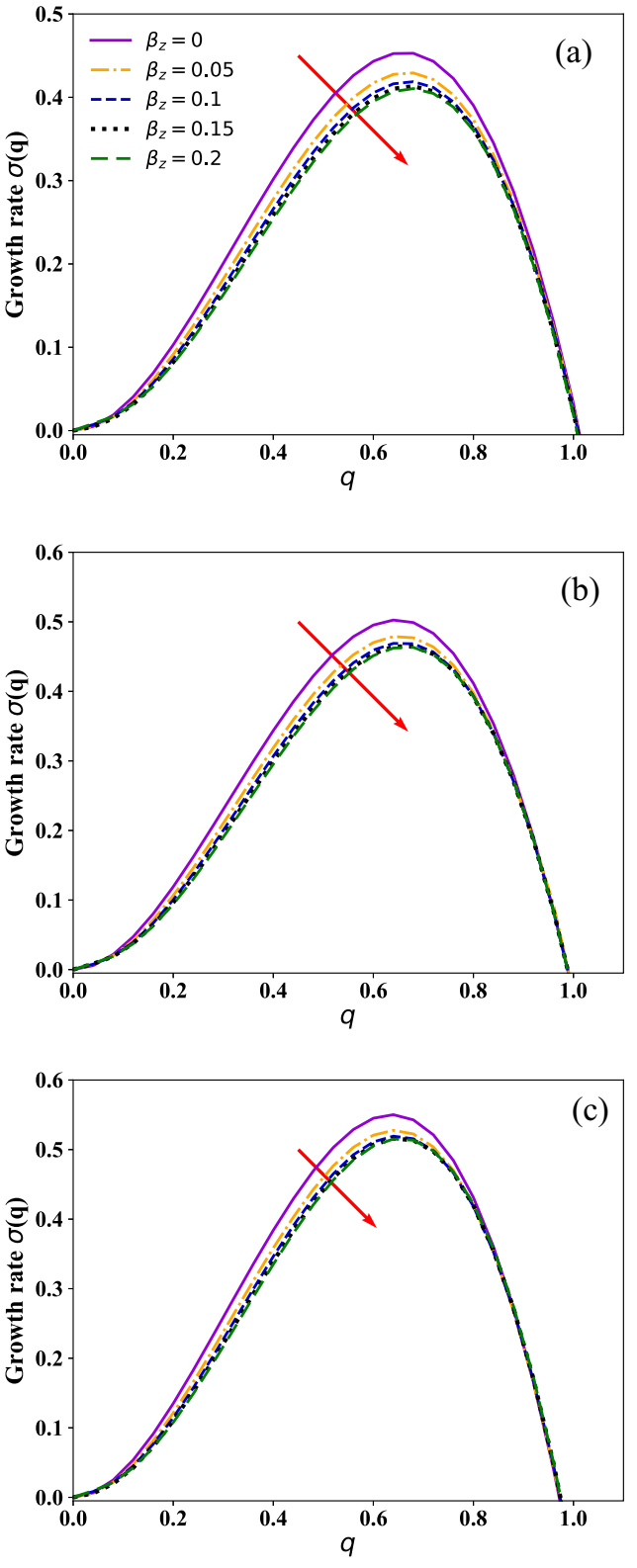

FIG. 16. Temporal growth rate $\sigma(q)$ vs wave number q for different streamwise slippery lengths: (a) $\beta_\theta = 0$, (b) $\beta_\theta = 0.1$, and (c) $\beta_\theta = 0.2$. Arrow represents the increase of the streamwise slippery effect, $\beta_z = [0, 0.05, 0.1, 0.15, 0.2]$.

length are shown in Fig. 15. Since the roles of small radius are more complex, in the numerical calculations $R = 1$ is used. Three values for the streamwise slippery length are given, including $\beta_z = 0$, $\beta_z = 0.1$, and $\beta_z = 0.2$. A similar variation of $\sigma(q)$ is displayed in the three figures. For a specified value of β_z, the transverse slippery effect has a dual effect on the surface instability. While the perturbation has a small value of wave number, the growth rate becomes larger with the increase of the β_θ, indicating that the transverse slippery effect destabilizes the surface instability. However, for the perturbation of a large wave number, the transverse slippery length plays a stabilizing role. Based on the energy analysis of Spaid and Homsy [5], it has been known that the flow in the θ direction due to the θ curvature removed energy for $q > 0.5$, and is partially responsible for determining the cutoff wave number. From the plots, it can be observed that the cutoff wave number indeed decreases with the increase of the transverse slippery length. The energy of flow in the ξ direction due to the θ curvature is a positive function of the slippery length, and therefore for a small wave number, especially for $q < 0.5$, the flow becomes more unstable while the transverse slippery length is larger.

In Fig. 16, the influence of the streamwise slippery length is shown for three different transverse slippery lengths β_θ. Comparing the three figures, it can be found that with a larger β_z, the growth rate is smaller for a given wave number, demonstrating that the streamwise slippery length plays a stabilizing role here, and the fingering spreading occurs in a longer time evolution. The foundation is consistent with the findings by Ma [49]. Comparing the three figures, one can also note that the cutoff wave number is almost unaffected by the streamwise slippery length, and the cutoff wave number decreases with the increase of the transverse slippery length.

VI. DISCUSSION AND CONCLUSIONS

In conclusion, we have studied the dynamics of a thin liquid film flowing down a slippery cylindrical surface. A lubrication model was briefly introduced that considered the wall slippage. The isotopic slippery effect and anisotopic slippery effect were both taken into consideration. The contact line instability of the falling film was investigated by numerical simulations and linear stability analysis. The influence of the slippery length, substrate curvature, and the thickness of the precursor layer were analyzed and the linear stability analysis had good agreement with the numerical simulations.

The traveling wave solutions provided insights into the three-dimensional flows, accompanied with fruitful results: First, the traveling speed of the flow is $c = (1 + b + b^2) + 3\beta_z(1 + b)$, which is proportional to the streamwise slippery length, and has no relationship with the transverse slippery length. The velocities obtained from the theoretical analysis were verified by numerical simulations. Second, the LSA demonstrated that the precursor film thickness played a stabilizing role in thin film flow, while the substrate curvature destabilized the flow.

The most important conclusion in this paper came from the investigation of the slippery effect. Unlike the destabilizing action of the slippery effect in the motion of thin film flows without dynamic contact lines [38,39,41], the effect of the slippery effect in the motion of dynamic contact lines was much more complex, especially for a cylinder of small radius ($R \leqslant 1$). The streamwise slippery length played a stabilizing role in the surface instability, and the effect became very small while the wave number of the perturbation was large. The transverse slippery length played a dual role in the surface instability due to the value of the wave number of the perturbation: The effect destabilized the surface instability while the wave number was small, and the effect changed to a stabilizing role while the wave number of the perturbation was large. These analyses provide some inspiration in such areas as petroleum engineering, mechanical engineering, coating industry, etc.

ACKNOWLEDGMENTS

We wish to acknowledge the support from the National Natural Science Foundation of China (Grants No. 11702162 and No. 11972375) and Key Technology R & D Program of Shandong Province (Grant No. 2019GHZ001). Chicheng Ma also wants to acknowledge the help of Dr. Zijing Ding from the University of Cambridge.

[1] R. V. Craster and O. K. Matar, Rev. Mod. Phys. **81**, 1131 (2009).
[2] F. Gallaire and P. T. Brun, Philos. Trans. R. Soc. A **375**, 20160155 (2017).
[3] S. M. Troian, E. Herbolzheimer, S. A. Safran, and J. F. Joanny, Europhys. Lett. **10**, 25 (1989).
[4] M. P. Brenner, Phys. Rev. E **47**, 4597 (1993).
[5] M. A. Spaid and G. M. Homsy, Phys. Fluids **8**, 460 (1996).
[6] J. A. Diez and L. Kondic, Phys. Rev. Lett. **86**, 632 (2001).
[7] A. Miyara, Int. J. Therm. Sci. **39**, 1015 (2000).
[8] M. Levy, M. Shearer, and T. P. Witelski, Eur. J. Appl. Math. **18**, 679 (2007).
[9] J. P. Pascal and S. J. D. D'Alessio, Int. J. Multiphase Flow **36**, 449 (2010).
[10] D. Takagi and H. E. Huppert, J. Fluid Mech. **647**, 221 (2010).
[11] Z. Ding and T. N. Wong, Int. J. Heat Mass Transf. **90**, 689-701 (2015).
[12] Z. Ding and T. N. Wong, Phys. Fluids **29**, 011701 (2017).
[13] Z. Ding, R. Liu, T. N. Wong, and C. Yang, Chem. Eng. Sci. **177**, 261 (2018).
[14] C. Ma, Int. J. Heat Mass Transf. **136**, 719 (2019).
[15] L. Luo, G. Zhang, J. Pan, and M. Tian, J. Hydrodyn., Ser. B **25**, 404 (2013).
[16] A. M. Frank and O. A. Kabov, Phys. Fluids **18**, 032107 (2006).
[17] M. Mittermaier, P. Schulze, and F. Ziegler, Int. J. Heat Mass Trans. **70**, 990 (2014).
[18] Q. Qiu, X. Zhu, L. Mu, and S. Shen, Int. J. Heat Mass Trans. **84**, 893 (2015).
[19] F. Sun, S. Xu, and Y. Gao, Front Chem. Sci. Eng. **6**, 322 (2012).
[20] J. Chen, R. Zhang, and R. Niu, Renew. Energ. **73**, 62 (2015).
[21] Q. Qiu, X. Zhang, S. Quan, X. Zhu, and S. Shen, Int. J. Heat Mass Trans. **124**, 943 (2018).

[22] S. Lin, Z. Zhang, X. Liu, K. Zhuang, and X. Li, Int. J. Heat Mass Trans. **117**, 465 (2018).
[23] Z. Ding, Z. Liu, R. Liu, and C. Yang, Int. J. Heat Mass Trans. **138**, 524 (2019).
[24] L. Kondic and J. Diez, Phys. Fluids **13**, 3168 (2001).
[25] L. Kondic, Siam Rev. **45**, 95 (2003).
[26] M. R. E. Warner, R. V. Craster, and O. K. Matar, J. Fluid Mech. **510**, 169 (2004).
[27] M. R. E. Warner, R. V. Craster, and O. K. Matar, Phys. Fluids **16**, 2933 (2004).
[28] T. S. Lin and L. Kondic, Phys. Fluids **22**, 052105 (2010).
[29] T. S. Lin, L. Kondic, and A. Filippov, Phys. Fluids **24**, 022105 (2012).
[30] L. C. Mayo, S. W. McCue, and T. J. Moroney, Phys. Rev. E **87**, 053018 (2013).
[31] P. D. Howell, J. Robinson, and H. A. Stone, J. Fluid Mech. **732**, 190 (2013).
[32] B. Hu and L. K. Sarah, J. Non-Newtom. Fluid Mech. **225**, 62 (2015).
[33] Z. Zheng, S. Shin, and H. A. Stone, J. Fluid Mech. **778**, 669 (2015).
[34] Y. E. Yu, Z. Zheng, and H. A. Stone, Phys. Rev. Fluids **2**, 074101 (2017).
[35] A. Münch and B. Wagner, Phys. D (Amsterdam, Neth.) **209**, 178 (2005).
[36] A. Samanta, C. Ruyer-Quil, and B. Goyeau, J. Fluid Mech. **684**, 353 (2011).
[37] A. Samanta, B. Goyeau, and C. Ruyer-Quil, J. Fluid Mech. **716**, 414 (2013).
[38] Z. Ding and Q. Liu, Phys. Rev. E **84**, 046307 (2011).
[39] Z. Ding, T. N. Wong, R. Liu, and Q. Liu, Phys. Fluids **25**, 064101 (2013).
[40] R. Liu and Z. Ding, Phys. Rev. E **95**, 053101 (2017).
[41] Y. Chao, Z. Ding, and R. Liu, Chem. Eng. Sci. **175**, 354 (2018).
[42] T. S. Wong, S. H. Kang, S. K. Tang, E. J. Smythe, B. D. Hatton, A. Grinthal, and J. Aizenberg, Nature (London) **477**, 443 (2011).
[43] P. Kim, T. S. Wong, J. Alvarenga, M. J. Kreder, W. E. Adorno-Martinez, and J. Aizenberg, ACS Nano **6**, 6569 (2012).
[44] D. Wu, L. Ma, F. Zhang, H. Qian, B. Minhas, Y. Yang, X. Han, and D. Zhang, Mater. Design **185**, 108236 (2020).
[45] X. Zhang, L. Sun, Y. Wang, F. Bian, Y. Wang, and Y. Zhao, Proc. Natl. Acad. Sci. USA **116**, 20863 (2019).
[46] W. Gao, J. Wang, X. Zhang, L. Sun, Y. Chen, and Y. Zhao, Chem. Eng. J. **381**, 122612 (2020).
[47] J. Jiang, J. Gao, H. Zhang, W. He, J. Zhang, D. Daniel, and X. Yao, Proc. Natl. Acad. Sci. USA **116**, 2482 (2019).
[48] F. Hecht, O. Pironneau, A. Le Hyaric, and K. Ohtsuka, FreeFem++ manual (2005), http://www.freefem.org/.
[49] C. Ma, J. Liu, S. Xie, and Y. Liu, Chem. Eng. Sci. **214**, 115418 (2020).
[50] Z. Ding, Z. Liu, R. Liu, and C. Yang, Chem. Eng. Sci. **199**, 342 (2019).
[51] R. Liu, X. Chen, and Z. Ding, Phys. Rev. E **97**, 013109 (2018).